CrystEngComm

Accepted Manuscript

ROYAL SOCIETY OF CHEMISTRY

www.rsc.org/crystengcomm

A facile one-pot hydrothermal synthesis of branched α-MnO_2 nanorods for supercapacitors application

Xiaohui Su,[†a] Xianfeng Yang, [†b] Lin Yu*[a], Gao Cheng [a], Huanhua Zhang [a], Ting Lin [a], Feng-Hua Zhao [a]

[a]School of Chemical Engineering and Light Industry, Guangdong University of Technology, Guangzhou, Guangdong, 510006, China

E-mail address: gych@gdut.edu.cn, suxiaohui4336@126.com

[b]Analytical and Testing Center, South China University of Technology, Guangzhou, 510641, China

*Corresponding author

School of Chemical Engineering and Light Industry, Guangdong University of Technology, Guangzhou, Guangdong, 510006, China

E-mail address: gych@gdut.edu.cn, suxiaohui4336@126.com.

TEL.: +862039322202

[†]Equal contribution to this work.

ABSTRACT

Branched α-MnO_2 nanorods are synthesized using a facile hydrothermal method without surfactants or templates. The formation of α-MnO_2 with different morphologies, including branched nanorods and nanorods with controllable length, is achieved by controlling the starting concentration of reactants. The morphology and structure of the branched α-MnO_2 nanorods are fully characterized and the growth mechanism is proposed based on the experimental observation. The novel structures presented here enrich the nanoscale community of α-MnO_2 material and enabling greater potential applications. The electrochemical properties of as-synthesized branched α-MnO_2 nanorods are also studied by cyclic voltammetry (CV) and

galvanostatic charge/discharge. The branched α-MnO_2 nanorods electrode shows a high specific capacitance of 182 F g^{-1} at the current density of 2 A g^{-1}, with a good rate capability (72.5% at 64 A g^{-1}) and an excellent cycling stability.

1. Introduction

Nowadays, high-energy and high-power-density energy-storage devices have attracted much attention due to the increasing demand for high-power applications such as electric vehicles and hybrid electric vehicles[1,2]. Supercapacitors, also known as electrochemical capacitors, exhibit many advantages such as greater power density, long cycle life, and higher energy density [3]. As is well known, the electrode materials are one of the most important parameters to determine the supercapacitor performance[4]. Three major electrode materials, such as metal oxides/hydroxides[5,6], carbonaceous materials[7] and conducting polymers[8], have been developed as possible supercapacitor electrodes. Among them, metal oxides are considered to be good electrode materials for their large specific capacitance and fast redox kinetics. RuO_2 shows the best supercapacitive properties due to its exciting specific capacitance[9], but high cost and toxicity properties hinder its practical application. Therefore, much effort has been devoted to transition metal oxides that possess the attractive advantages of low cost, abundance, environmentally friendly nature, and special high capacity.

Manganese oxides (MnO_2), as transition metal oxides, have been investigated as electrode materials for supercapacitor applications because of their abundance, superior environmental benignity and especially their high theoretical capacity (1110 F g^{-1}) [10,11]. MnO_2 exists in several crystallographic structures, such as α, β, γ and δ, which are made of the basic unit [MnO_6] octahedral with different connectivity[12].

Generally, the specific capacitance of MnO_2 greatly depends on the crystalline structure and morphology[13]. Among the different phases of MnO_2, α-MnO_2 (2×2 tunnel structure as illustrated in Fig.1 showed higher capacitance compared with other phases due to its wide tunnel size (0.46 nm) and large surface area[14]. Therefore, intensive studies on the electrochemical property investigations of MnO_2 supercapacitor are now focused on α-MnO_2.

Recently, α-MnO_2 nanostructures with different morphologies have been successfully synthesized, including nanorods[16], nanowires[17], nanotubes[18], hollow spheres[19], nanoflowers[20], nanobelts[21], and nanosheets[22]. However, to the best of our knowledge, there are few reports on the successful synthesis branched MnO_2 nanostructures with one dimensional (1D) nanostructures as building blocks. Although some branched nanostructures of β-MnO_2[23] and ε-MnO_2[15] have been achieved, there is still a big challenge to fabricate branched α-MnO_2 nanorods through a facile and convenient method.

Herein, we synthesize branched α-MnO_2 nanorods via a facile one-pot hydrothermal method without using any without using any surfactants or templates. The effect of the reaction time and the starting concentration of reactants on the microstructure and morphology of samples are also observed systemically. We try to understand the growth process of the α-MnO_2 multipods through carefully analyzing the resulting structures. In addition, the electrochemical performances of the branched α-MnO_2 nanorods are presented and discussed.

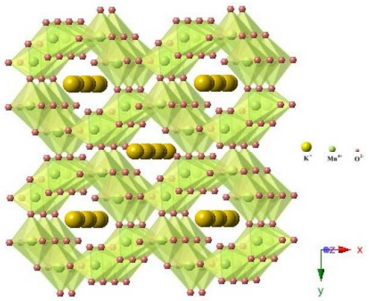

Figure 1 Structure of α-MnO_2

2. Experimental

2.1 Material synthesis

All the chemical reagents were analytical grade without further purification. In a typical hydrothermal synthesis of the branched α-MnO_2 nanorods, the solution was prepared by adding 0.002 M of $MnSO_4 \cdot H_2O$ and 0.005 M of $KMnO_4$ into 60 mL distilled water. After stirring for 15 minutes, the solution was transferred into a Teflon-lined stainless steel autoclave and maintained at 140°C for 12 hours in an oven. After the reaction, the autoclave was taken out and cooled to room temperature. The as-synthesized sample was washed by deionized water and absolute ethanol, and dried at 60°C for 6 h. A set of experiments were conducted via adjusting reaction time and concentration, and the preparation process were similar to those used in the above. With regard to the different concentrations for convenience, the concentration of $KMnO_4$ was used as the reference, the amount of $MnSO_4 \cdot H_2O$ was adjusted according to the stoichiometry (2:5) of α-MnO_2. The concentration of $KMnO_4$ used in the experiment was 0.05 and 0.3M.

2.2 Characterization

X-ray powder diffraction (XRD) was performed on a Brucker D8 X-ray diffractometer operating at a power of 40 kV × 40 mA with Cu Kα radiation. All the XRD patterns were collected at room temperature with a 0.01° step size in 2θ, from 2θ

= 10º to 80º. The field emission scanning electron microscopy (FESEM) images were taken on a Hitachi S4800 microscope operated at 15 kV. The transmission electron microscopy (TEM), selected area electron diffraction (SAED) patterns and high-resolution transmission electron microscopy (HRTEM) was performed on a FEI Tecnai G20 TEM at an acceleration voltage of 200 kV. The BET surface area was determined by a multipoint N_2 adsorption-desorption method in liquid N_2 (-196 ^oC) with a GEMINI V 2380 surface area analyzer. Samples were treated under 200^oC in N_2 atmosphere for 4h to evacuate the physisorbed moisture before measurement.

2.3 Electrochemical Measurement

The working electrode of electrochemical measurement was formed by mixing 75 wt% the as-synthesized sample, 20 wt% acetylene black and 5% PVDF in NMP solvent. The mixture was placed in an ultrasonic bar for about 1 h to make a homogeneous solution and subsequently was pasted onto a 1 cm^2 of carbon fiber paper (CFP). The electrode was dried at 110 ^oC under vacuum for 10 hours. The loading density is about 0.8 mg cm^{-2}. The electrochemical characteristics were studied by cyclic voltammetry (CV) and galvanostatic charge/discharge using a three-electrode cell in N_2-saturated 1.0 M Na_2SO_4 aqueous solution. The as-synthesized product was employed as the working electrodes, Pt electrode as the counter electrode and saturated calomel electrode (SCE) as the reference electrodes. The instrument used for electrochemical measurements was an electrochemical work station (PGSTAT 302N). The obtained galvanostatic charge–discharge curves were used for the calculation of the specific capacitance (C) according to the following equation:

$$C = \frac{It}{m\Delta V} \quad (1)$$

Where I and t are denoted to the constant discharge current and the time, m represents

the mass of electroactive material, and ΔV is the potential window of cycling.

3. Results and discussion

The phase and crystallinity of the as-synthesized material were tested by X-ray powder diffraction (XRD) as shown in Fig.2a. All the diffraction peaks can be exclusively relegated to the α-MnO_2 (JCPDS 44-0141, tetragonal symmetry with *I*4/m space group and lattice constants of a = 9.7847 Å, b = 9.7847 Å and c = 2.6830 Å), and no characteristic peaks can be observed for the impurities, demonstrating that the material synthesized is pure α-MnO_2. The morphology was observed by FESEM images, as shown in Fig. 2b. It can be seen that the products are high-yield branched α-MnO_2 nanorods. Most of the nanorods have a diameter ranging from 40 to 70 nm with a high aspect ratio as shown in Fig.3a-c. The connections at the junction can be clearly observed, which indicates that the branches are formed through self-assembly of 1D nanorods. Most of the tips/ends of the 1D nanorods are terminated by a sword-like shape.

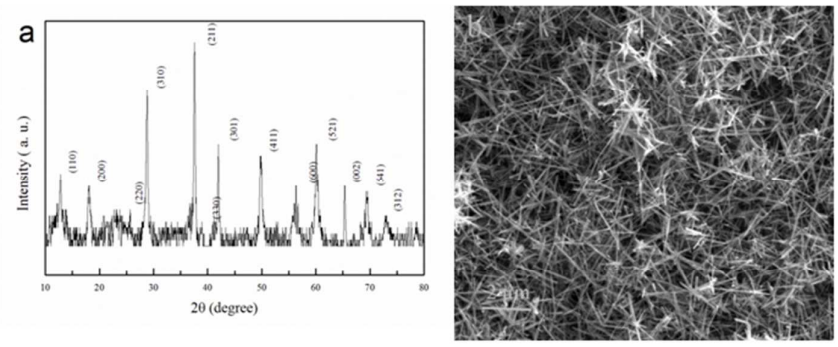

Fig.2 (a) XRD patterns and (b) the FESEM image of the prepared material obtained by using 0.005 M of $KMnO_4$ at a reaction time of 12 h.

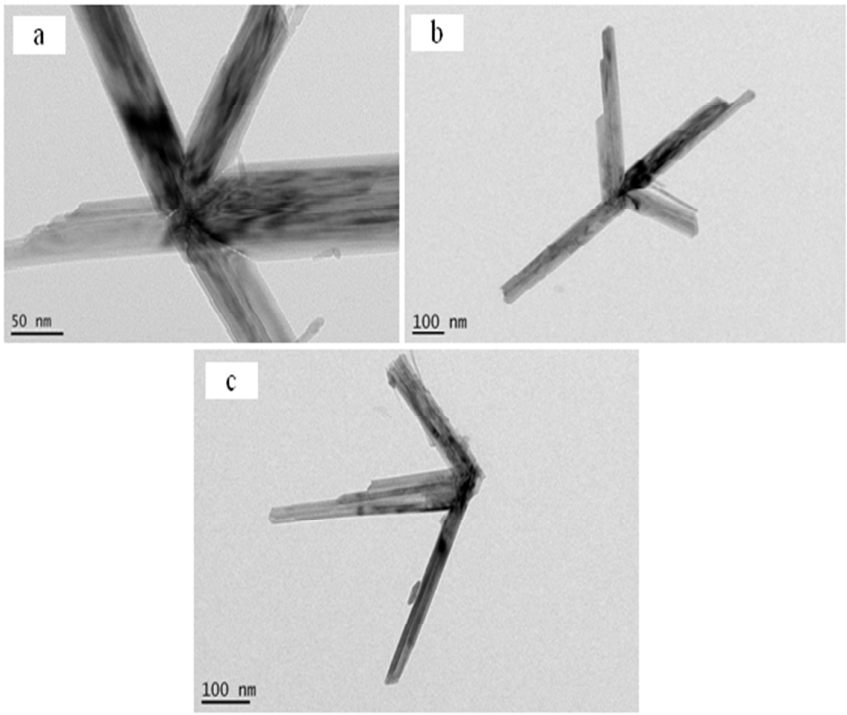

Fig.3 (a-c) TEM images of the branched α-MnO_2 nanorods with different shapes

TEM images of two branched nanorods and the corresponding SAED patterns are presented in Fig.4. Selected area electron diffraction (SAED) was carried out to characterize the structure of the as-prepared branched nanorods. It shows that all the straight nanorods are single crystal and the diffraction patterns can be indexed to the tetragonal symmetry of α-MnO_2, consistent with the XRD results (Fig. 2a). The two SAED patterns taken from the tow corresponding branches can be indexed with the same zone axis of [111]. The SAED pattern of the conjunction part, which is a combination of above two SAED patterns, showed the diffraction spots of (1-21) and (-211) from above two SAED patterns were overlapped. It suggests that the two branched nanorods shared their {211} lattice planes as illustrated in the schematic model in Fig 4(a). In another word, there are {211} twin planes within this branched structure. HRTEM image of the conjunction part and the corresponding FFT patterns shown in Fig 5 further confirmed that the branches are formed by self-assembly of

well-crystallized nanorods through a {211} twinned structure. The tunnel structure presented in the schematic model of branched α-MnO_2 nanorods in Fig 4(a) could provide more electron/ ion paths and rapid transport of the charge carriers.

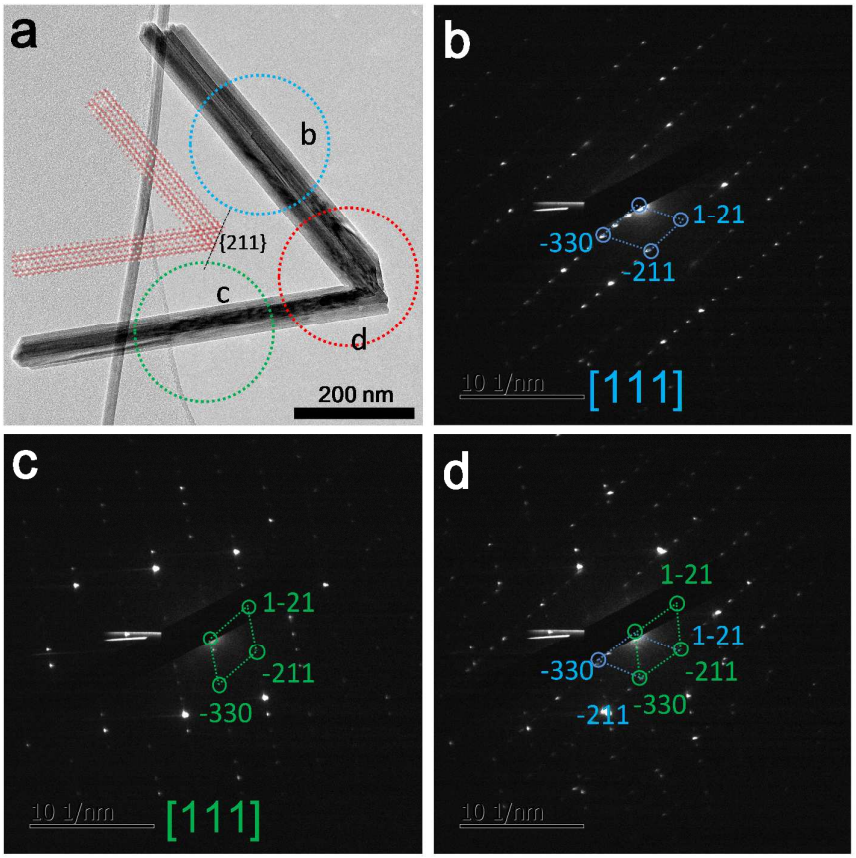

Fig.4 (a) TEM images of two branched nanorods with a schematic model, (b, c) and (d) the corresponding SAED patterns taken from the circle area of b, c and d in (a).

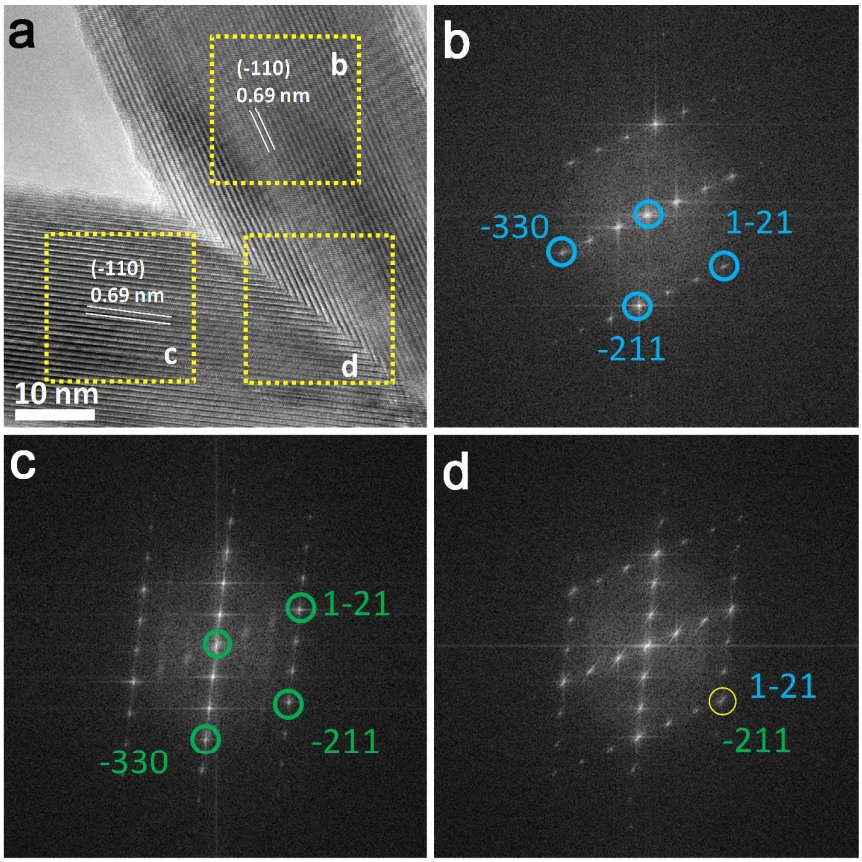

Fig.5 (a) HRTEM images of the conjunction part of the branched nanorods in Fig 4a, (b, c) and (d) the corresponding FFT patterns taken from the area of b, c and d in (a).

We have found that the concentration of the starting material influence the final morphology of product. Fig.6 shows the SEM images of α-MnO_2 structures obtained at a higher concentration of $KMnO_4$. When increasing the concentration of $KMnO_4$ to 0.05 M, the morphology of α-MnO_2 changes to nanorods, as shown in Fig.6a. The length of the as-synthesized α-MnO_2 nanorods are in the range of 1 to 2 μm. With a concentration of 0.3 M $KMnO_4$, the length of the nanorods becomes shorter (0.2 to 0.6μm) and their morphology proportion to the whole product decreased (Fig.6b). The above results demonstrate that the concentration of the starting material plays an important role in synthesizing the branched α-MnO_2 nanorods.

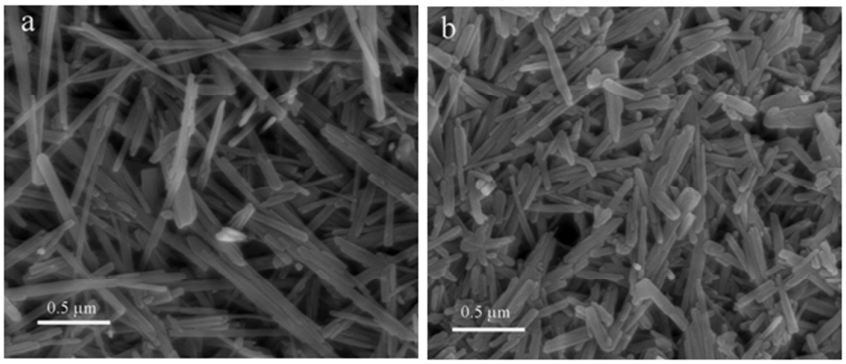

Fig.6 FESEM images of the prepared material obtained for 12 h under different concentrations: (a) 0.05 M of $KMnO_4$ and (b) 0.3 M of $KMnO_4$.

In order to understand the formation mechanism of the branched α-MnO_2 nanorods, time-dependent experiments were carried out at 140 ^oC. Detailed time-dependent evolutions of morphology and crystallinity were studied by FESEM and XRD measurements, which are shown in Fig.7. When the reaction time was 0.5 h, the product consists of δ-MnO_2 with the flower-like morphology. Prolonging reaction time to 2 h, the size of nanoflowers increases a little. After reacting for 4 h, a lot of branched α-MnO_2 nanorods grow from the flowers, indicating the δ-MnO_2 nanoflowers are in the form of a metastable phase under the reaction condition.

Based on the above experiments, the formation mechanism of the branched α-MnO_2 nanorods is proposed. In the very beginning, nanoflowers made of δ-MnO_2 nanosheets can be formed with fast nucleation-growth kinetics once the reaction is initiated. Since δ-MnO_2 nanosheets are not stable under reaction condition and they tend to transform into the stable α-MnO_2 nuclei followed by a branching growth process. This phase transition process continues until all the nanosheets are consumed. The oriented-attachment mechanism is proposed to explain the branched α-MnO_2 growth process, which could efficiently decrease the total energy of the system. On the basis of the above discussions, it sounds reasonable to conclude that the reactions

follow a nucleation-dissolution-recrystallization-oriented attachment mechanism.

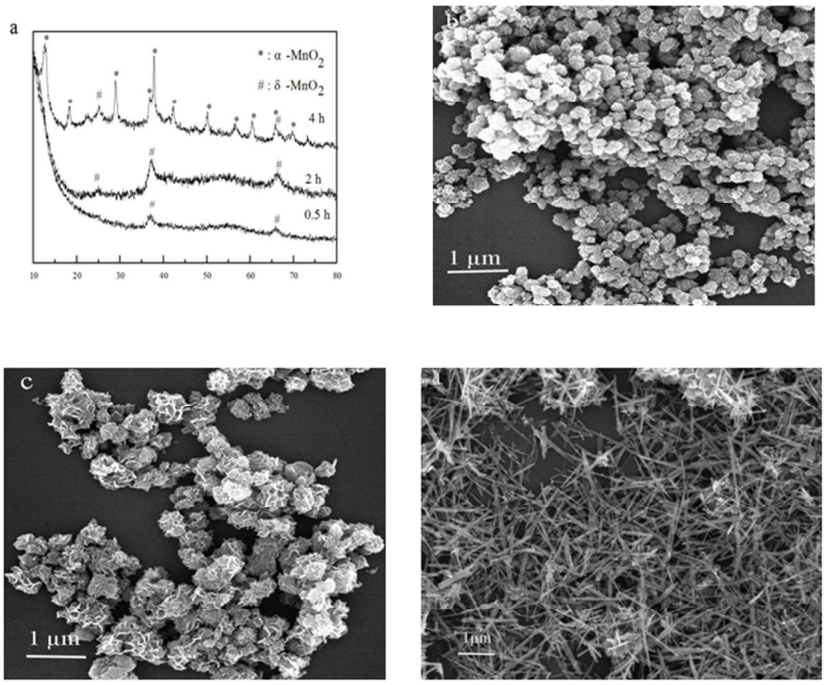

Fig.7 (a) X-ray diffraction (XRD) of the as-prepared materials obtained by using 0.005 M of $KMnO_4$ treated for different reaction times, i.e., 0.5, 2, and 4 h. (B-D) Corresponding typical SEM images of the products.

To investigate the surface area and pore structure of the branched α-MnO_2 nanorods, the N_2 adsorption-desorption isotherms (BET) were taken, and the result obtained is displayed in Fig.8. The isotherm of sample can be classified as type IV with Type H3 loop according to the IUPC classification, typical of mesoporous materials. The hysteresis loop of the branched α-MnO_2 nanorods located in the P/P_0 range of 0.8–1 is very small and almost no plateaus is observed, mainly due to the existence of large mesopores and macropores in the sample[24]. The BET surface area and cumulative pore volume of the sample are determined to be 41.8 $m^2 g^{-1}$ and 85 $cm^3 g^{-1}$, respectively. As shown by BJH analysis (inset in Fig.8), the pore size distributions of the sample are mainly in the diameter ranges of 2–10 nm and >10 nm. It should be noted that this multi-peak distribution including both mesopores and

macropores may greatly improve the accessibility of the material to electrolyte ions and the diffusion of electrons by providing an efficient transport pathway and more adsorption sites in the interior of the sample[25]. The high BET surface area and porous features of the branched nanostructures can increase surface activity and electrolyte infiltration in supercapacitors.

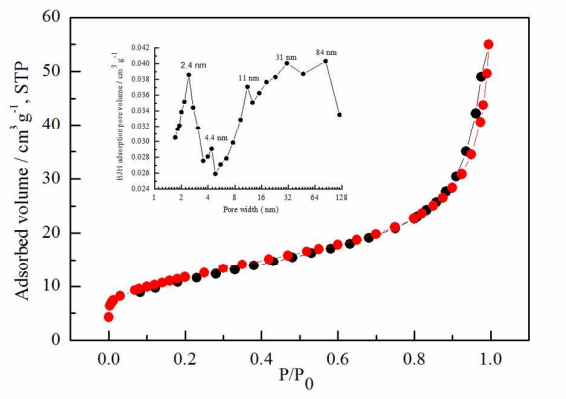

Fig.8 N_2 adsorption-desorption isotherms of the branched α-MnO_2 nanorods, and the inset shows the BJH pore-size distribution.

To explore the potential applications of the branched α-MnO_2 nanorods, it was fabricated into supercapacitor electrode and characterized with CV and galvanostatic charge/discharge measurements. Fig.9 shows CVs of the branched α-MnO_2 nanorods in N_2-saturated 1 M Na_2SO_4 solution with the potential range of 0-1 V (*vs.* SCE) at different scan rates ranging from 5 to 500 mV s^{-1}. It can be seen that the CV curves are close to rectangular shape even at a higher scan rate of 500 mV s^{-1}, indicating good high-rate capability, efficient intralayer charge transfer and ideally capacitive characteristic of the sample. The CV curves of the branched α-MnO_2 nanorods electrode show no peaks between 0 to 1 V, which suggests that the electrode is charged and discharged at a pseudo-constant rate over the complete voltammetric cycle originating from the following reactions:

$$(MnO_2)_{surface} + C^+ + e^- \longleftrightarrow (MnOOC)_{surface} \quad (2)$$

$$MnO_2 + C^+ + e^- \longleftrightarrow MnOOC \quad (3)$$

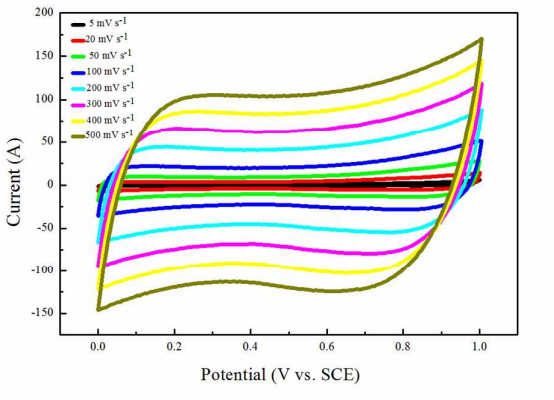

Fig.9 Cyclic voltammograms of the branched α-MnO_2 nanorods at different scan rates.

Fig.10 shows the galvanostatic charge-discharge curves of the branched α-MnO_2 nanorods in 1 M Na_2SO_4 solution at various current densities with the potential range of 0-1 V. It can be seen that all the charge–discharge curves are linear and symmetrical, demonstrating its ideal pseudocapacitive behavior, which is in good agreement with the CV data in Fig.9. The SC of the branched α-MnO_2 nanorods at different current densities can be calculated based on the discharge curves in Fig.10a and collected in Fig.8b. The SC of the branched α-MnO_2 nanorods was calculated to be 182, 182, 164, 164, 150 and 132 F g^{-1} at the current densities of 2, 4, 8, 16, 32 and 64 A g^{-1}, respectively. Even at a current density as high as 64 A g^{-1}, it still retained a high SC of 132 F g^{-1}. This value is much greater than those reported in previous work such as MnO_2 thin film (70.4 F g^{-1} at a current density of 20 A g^{-1}) [26], 3-D porous coral-like MnO_2 thin-film (96 F g^{-1} at a current density of 20 A g^{-1})[27] and mesoporous MnO_2 nanowire array (84 F g^{-1} at a current density of 12 A g^{-1})[28]. It is well accepted that rate capability is an important factor for supercapacitors in high power

applications[3]. The branched α-MnO_2 nanorods electrode preserves 72.5% of its SC value when the charge/ discharge rate is increased from 2 to 64 A g^{-1}, indicating good rate capability.

The excellent supercapacitive properties of the branched α-MnO_2 nanorods electrode can be attributed to the novel textural morphology and crystal structure. First of all, the branched nanorods afford a high surface area for high capacitance and point contacts between the branched α-MnO_2 nanorods provide more electron transport pathways and low contact resistance at the junction[29,30]. Secondly, the crystal structure of the prepared branched α-MnO_2 nanorods is constructed by double chains of [MnO_6] forming 2×2 tunnel with a cavity as large as 0.46 nm, which has the potential to facilitate the intercalation of cations into MnO_2. Finally, the nanorod structure can provide short diffusion path lengths for both ions and electrons.

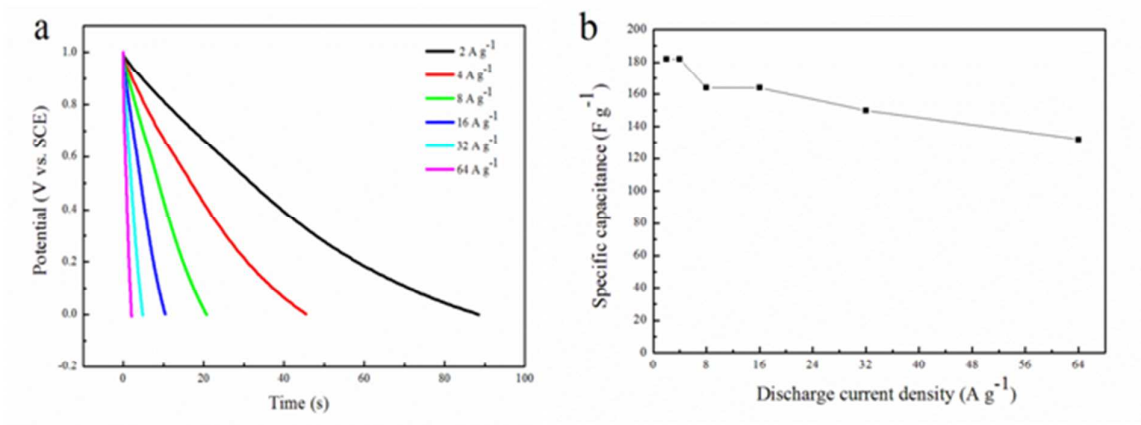

Fig.10 (a) Charge/discharge curves of the branched α-MnO_2 nanorods in the potential range from 0 to 1.0 V at different current densities. (b) Specific capacitance of the branched α-MnO_2 nanorods at different charge/discharge current densities.

The long-term cycle stability of electrode materials is one of the most critical

factors for their practical applications. The long-term cycling stability of the branched α-MnO_2 nanorods was examined by charge–discharge cycling at a constant current density of 8 A g^{-1} for 2000 cycles, the variation in SC as a function of cycle number is depicted in Fig. 11. It can be seen that the SC decreases slightly in the first 500 cycles and then increases slightly with increasing cycle number. As revealed from the above data, there is no decrease in SC value over 2000 cycles, showing a good cyclability of the branched α-MnO_2 nanorods electrode. This result highlights the capability of the branched α-MnO_2 nanorods electrode to meet the requirements of both long cycle lifetime and good rate capability, which are important for the practical energy storage devices.

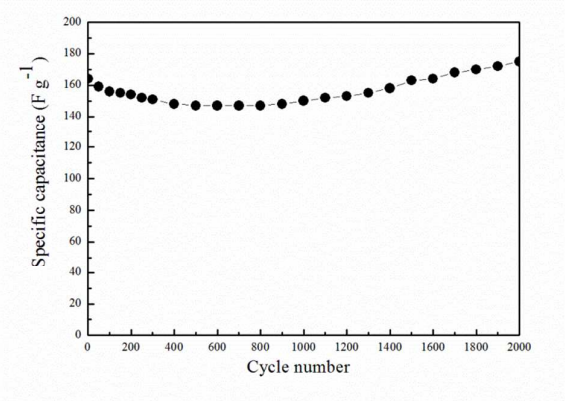

Fig.11 Cycle life of the branched α-MnO_2 nanorods at the current density of 8 A g^{-1} in 1 M Na_2SO_4 solution.

4. Conclusions

In this paper, we successfully synthesized the branched α-MnO_2 nanorods by a facile hydrothermal method without any surfactants or templates. The α-MnO_2 with different morphologies, including branched nanorods and nanorods with controllable length, is prepared by controlling the starting concentration of reactants. The growth process of the branched α-MnO_2 nanorods is evolved from δ-MnO_2 nanosheets as proved by SEM and XRD results in various stages during the growth. The branched

α-MnO_2 nanorods electrode shows a specific capacitance of 182 F g^{-1} at the current density of 2 A g^{-1}, a good rate capability with 72.5% retention at 64 A g^{-1} and an excellent cycling stability. The excellent supercapacitive properties of the branched α-MnO_2 nanorods electrode may be attributed to the novel textural morphology and crystal structure. The novel structures presented here enrich the nanoscale community of α-MnO_2 material and enabling greater potential applications.

Acknowledgments

This work was supported by Natural Science Foundation of Guangdong (10251009001000003), Scientific Program of Guangzhou (2010Z1-E061) and 211 Project of Guangdong Province.

References

1 X. H. Xia, Y. Q. Zhang, D. L. Chao, C. Guan, Y. J. Zhang, L. Li, X. Ge, I. M. Bacho, J. P. Tu and H. J. Fan, *Nanoscale*, 2014, **6**, 5008–5048.

2 X. H. Lu, M. H. Yu, G. M. Wang, Y. X. Tong and Y. Li, *Energy Environ. Sci.*, 2014, **7**, 2160–2181.

3 G. P. Wang, L. Zhang and J. J. Zhang, *Chem. Soc. Rev.*, 2012, **41**, 797–828.

4 P. J. Hall, M. Mirzaeian, S. I. Fletcher, F. B. Sillars, A. J. R. Rennie, G. O. Shitta-Bey, G. Wilson, A. Cruden and R. Carter, *Energy Environ. Sci.*, 2010, **3**, 1238–1251.

5 H. Jiang, C. Z. Li, T. Sun and J. Ma, *Nanoscale*, 2012, **4**, 807–812.

6 H. Jiang, C. Z. Li, T. Sun and J. Ma, *Chem. Commun.*, 2012, **48**, 2606–2608

7 Z. J. Zhu, Y. J. Hu, H. Jiang and C. Z. Li, *J. Power Sources*, 2014, **246**, 402-408

8 T. Y. Liu, L. Finn, M. H. Yu, H. Y. Wang, T. Zhai, X. H. Lu, Y. X. Tong and Y. Li, *Nano Lett.*, 2014, **14**, 2522−2527.

9 C. C. Hu, K. H. Chang, M. C. Lin and Y. T. Wu, *Nano Lett.*, 2006, **6**, 2690-2695.

10 H. Z. Chi, Y. W. Li, Y. X. Xin and H. Y. Qin, *Chem. Commun.*, 2014, **50**, 13349—13352.

11 B. Yin, S. W. Zhang, Y. Jiao, Y. Liu, F. Y. Qu and X. Wu, *CrystEngComm*, 2014, **16**, 9999–10005.

12 S. L. Suib, *Accounts. Chem. Res.*, 2008, **41**, 479-487.

13 L. L. Yu, J. J. Zhu and J. T. Zhao, *J. Mater. Chem. A*, 2014, **2**, 9353–9360.

14 J. J. Shao, W. Y. Li, X. Y. Zhou and J. Q. Hu, *CrystEngComm*, 2014, **16**, 9987–9991.

15 Y. S. Ding, X. F. Shen, S. Gomez, H. Luo, M. Aindow and S. L. Suib, *Adv. Funct. Mater.*, 2006, **16**, 549–555.

16 Y. Cao, Z. K. Wei, J. He, J. Zang, Q. Zhang, M. S. Zheng and Q. F. Dong, *Energy Environ. Sci.*, 2012, **5**, 9765.

17 X.H. Su, L. Yu, G. Cheng, H.H. Zhang, M. Sun, L. Zhang, J.J. Zhang, *Applied Energy*, 2014, **134**, 439.

18 L. H. Li, C. Y. Nan, J. Lu, Q. Peng and Y. D. Li, *Chem. Commun.*, 2012, **48**, 6945.

19 D. Y. Li, J. Yang, W. X. Tang, X. F. Wu, L. Q. Wei and Y. F. Chen, *RSC Adv.*, 2014, **4**, 26796.

20 G. A. M. Ali, L. L. Tan, R. Jose, M. M. Yusoff and K. F. Chong, *Mater. Res. Bull.*, 2014, **60**, 5.

21 W. Y. Li, K. B. Xu, L. An, F. R. Jiang, X. Y. Zhou, J. M. Yang, Z. G. Chen, R. J. Zou and J. Q. Hu, *J. Mater. Chem. A*, 2014, **2**, 1443.

22 L. Wei, C. Q. Li, H. B. Chu and Y. Li, *Dalton Trans.*, 2011,**40**, 2332.

23 D. S. Zheng, Z. L. Yin, W. M. Zhang, X. J. Tan and S. X. Sun, *Cryst. Growth Des.,* 2006, **6**, 1733-1735.

24 L. Chen , N. Y. Gu , R. Ding, L. Qi and H. Y. Wang, *J Solid State Electrochem*,

2013, **17***,* 2579.

25 M. Sawangphruk, P. Srimuk, P. Chiochan, A. Krittayavathananon, S. Luanwuthi and J. Limtrakul, *Carbon,* 2013, **60**, 109.

26 D. D. Zhu, Y. D. Wang, G. L. Yuan and H. Xia, *ChemComm*, 2014, **50**, 2876.

27 Y. Zhao, P. Jiang and S. S. Xie, *J Power Sources*, 2013, **239**, 393.

28 C. L. Xu, Y. Q. Zhao, G. W. Yang, F. S. Li and H. L. Li, *Chem Commun*, 2009, **48**, 7575.

29 C. W. Cheng and H. J. Fan, *Nano Today*, 2012, **7**, 327.

30 D. P. Dubal, J. G. Kim, Y. M. Kim, R. Holze and W. B. Kim, *Energy Technol*., 2013, **1**, 125.

Graphical Abstract

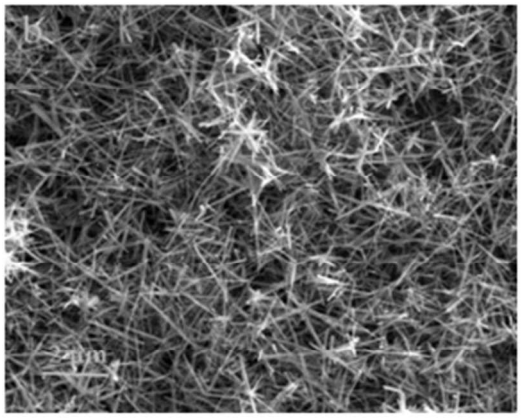

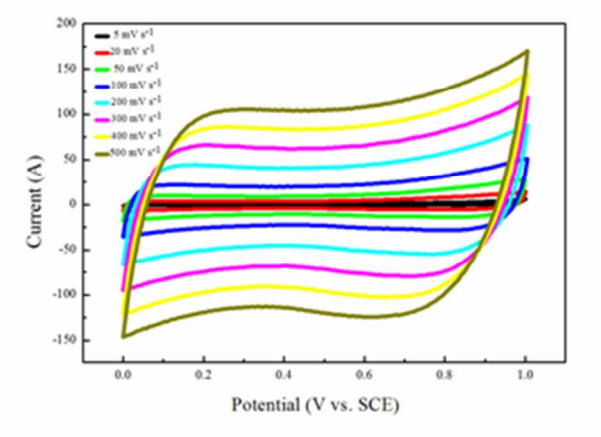

Branched α-MnO_2 nanorods are synthesized using a facile, green and effective one-pot hydrothermal approach without surfactants or templates. The branched α-MnO_2 nanorods electrode exhibited good supercapacitive properties due to its novel textural morphology and crystal structure.